Additive Manufacturing 124 (2026) 105229

Contents lists available at ScienceDirect

Additive Manufacturing

journal homepage: www.elsevier.com/locate/addma

Influence of substrate microstructure on defect formation during Al alloy laser powder bed fusion

Da Guo [a,b,*], Chengbo Zhu [c], Shishira Bhagavath [a,b], Rubén Lambert-Garcia [a,b], Sebastian Marussi [a,b], Marta Majkut [d], Alexander Rack [d], Federico Sket [e], Steven Van Petegem [f], Dmitry G. Eskin [c], Iakovos Tzanakis [g], Peter D. Lee [a,b,*], Chu Lun Alex Leung [a,b,*]

[a] UCL Mechanical Engineering, University College London, WC1E 7JE, UK
[b] Research Complex at Harwell, Harwell Campus, Didcot OX11 0FA, UK
[c] Brunel Centre for Advance Solidification Technology (BCAST), Brunel University of London, UB8 3PH, UK
[d] ESRF - The European Synchrotron, Grenoble 38000, France
[e] Madrid Institute for Advanced Studies of Materials (IMDEA Materials Institute), C/Profesor Aranguren s/n, Madrid 28040, Spain
[f] Laboratory for Condensed Matter, PSI Center for Photon Science, Villigen 5232, Switzerland
[g] School of Engineering, Computing and Mathematics, Oxford Brookes University, Oxford OX33 1HX, UK

ARTICLE INFO

Keywords:
Laser powder bed fusion
Synchrotron X-ray imaging
Microstructure
Intermetallics
Defects

ABSTRACT

Laser powder bed fusion (PBF-LB) produced aluminium alloy components have attracted growing attention over the past two decades due to their lightweight nature and excellent thermal and corrosion properties. However, few studies have examined the impact of substrate composition and microstructure. Using a high-performance Al-Ni-Ce-Mn-Fe alloy (PA1) designed for additive manufacturing, we performed a series of single-track PBF-LB experiments on as-cast PA1 and as-rolled Al6061 substrates to study their impact on track quality. Microstructural analysis shows that, in optimal conditions, PBF-LB of PA1 produces very fine eutectic cells (~200 nm) without defects. Conversely, the as-cast PA1 substrate contains large columnar intermetallics, which have a strong influence on defect formation during PBF-LB during initial layers. Such influence diminishes with increasing build height due to microstructure homogenisation. However, the identified intermetallic-induced (IM) pore formation suggests a broader relevance beyond the present system, such as alloys form intermetallic under AM conditions or additive repair. We reveal and quantify the effects of print parameters and substrate microstructure on defect formation during PBF-LB of PA1 using high-speed synchrotron X-ray imaging. Our results show a new defect type, termed intermetallic-induced pores, arising from interactions between the keyhole and the pre-existing intermetallics. By quantifying different melting modes and defect types, we establish a process map and propose defect-lean printing strategies for PBF-LB of PA1.

1. Introduction

Laser powder bed fusion (PBF-LB) is one of the prominent additive manufacturing (AM) technologies that allows the fabrication of highly complex-shaped metallic components layer by layer [1]. Owing to its short lead time, high material yield, and exceptional design flexibility, PBF-LB of aluminium alloys has attracted increasing interest, particularly for aerospace and autosport applications. Among Al alloys, AlSi10Mg remains the most widely used, due to its excellent printability and high strength-to-weight ratio [2,3]. However, the tensile yield strength of PBF-LB AlSi10Mg is limited to less than 300 MPa [4] and the working temperature is limited to 200°C. Recently, high-strength aluminium alloys have been explored to achieve superior mechanical properties [4,5]. However, these high-strength alloys suffer from high cracking susceptibility [6].

To achieve a high-performance Al alloy for AM applications with low cracking susceptibility and high strength, we designed a near-eutectic Al alloy (designated as PA1) based on the Al-Ni-Ce-Mn-Fe alloy system [7]. The design strategy, detailed in [7], involves narrowing the freezing range (2.8°C) and reducing solidification contraction through added

* Corresponding authors at: UCL Mechanical Engineering, University College London, WC1E 7JE, UK.
E-mail addresses: da.guo@ucl.ac.uk (D. Guo), peter.lee@ucl.ac.uk (P.D. Lee), alex.leung@ucl.ac.uk (C.L.A. Leung).

https://doi.org/10.1016/j.addma.2026.105229
Received 20 January 2026; Received in revised form 28 April 2026; Accepted 4 May 2026
Available online 5 May 2026

alloying elements (such as transition metals and rare earth elements with near eutectic compositions) with low diffusivity and solubility [8]. Previous studies have confirmed that PA1 exhibits an ultra-fine microstructure, coupled with low residual stresses and superior mechanical properties in as-built directed energy deposition (DED) AM components [9].

Under the slow cooling rates of conventional casting (< 78 C°/s), PA1 forms coarse columnar intermetallic phases dispersed within an aluminium eutectic matrix. When building on as-cast PA1 substrates, those intermetallics have limited effect on the deposited materials under DED conditions [9]. During DED, the high heat input (10^5 J/m) forms a large melt pool and dissolves the intermetallic phases. However, PBF-LB operates at cooling rates two orders of magnitude higher than DED [10], with much less time for complete dissolution of these intermetallics. Although the role of intermetallic phases in pore formation during casting is relatively well understood [11,12], their effect on PBF-LB builds remains largely unexplored.

In this study, we applied *in situ* high-speed synchrotron X-ray imaging to capture the melt pool dynamics and defect formation mechanisms during PBF-LB of PA1 built on different substrates under industrially relevant conditions. Our results reveal, for the first time, a novel defect formation mechanism in PBF-LB directly induced by the large intermetallic phases in the as-cast PA1 substrates. Based on these findings, we establish a process map for PA1 and propose optimised defect-lean printing parameters, thereby advancing the development of high-strength, crack-resistant Al alloys for AM.

2. Methods

2.1. Materials

A custom designed Al alloy powder feedstock (namely PA1) was alloyed and cast at Brunel University of London, UK (for details see [7]) and then ultrasonically atomized at AMAZEMET (Warsaw, Poland). Its chemical composition is listed in Table 1. Two types of substrates were selected for comparison, one from as-cast PA1 ingots and the other was machined from as-rolled Al6061 plate (chemical composition is given in Table 2).

2.2. In situ synchrotron imaging during PBF-LB process

The PBF-LB production parameters were designed to cover a broad range of imparted specific energy (E_s), with a laser power (P) of 200–500 W and scan speed (v) of 250–2000 mm/s. The imparted specific energy ($E_s = \frac{P}{\sqrt{vd}}$ $(Js^{1/2}/mm)$, where d is the laser beam diameter) is detailed in [13] and was used to reveal causal relationships between the process parameter and defect formation.

The experiments were performed using two bespoke PBF-LB process replicators: (i) the Quad-laser *in situ* and operando process replicator (Quad-ISOPR) [14,15] was used for the PA1 substrate (0.5 mm through-thickness and 15 mm height) sandwiched between two glassy carbon plates, see Fig. 1. The Quad-ISOPR is equipped with an industrial multi-laser scanning head and optics, enabling processing under conditions representative of industrial-level PBF-LB. Although the chamber size limits sample dimensions and long-range thermal accumulation, the identified defect formation mechanisms and relative process window remain relevant to commercial PBF-LB systems. The laser spot size of Quad-ISOPR was 80 μm. The powder was automatically deposited with a layer thickness of ~ 60 μm. (ii) The operando MiniSLM device [16] with a laser spot size of 45 μm was used for Al6061 substrate with a groove (0.5 mm through-thickness and 60 μm height) to create a powder bed. In both cases, argon shielding gas was used. The sample was printed under a flowing high-purity argon gas with flow rate of ~4 L/min. All *in situ* synchrotron X-ray imaging experiments were carried out at the ESRF – The European Synchrotron (France) imaging beamline ID19 (beamtime proposals ME-1573 and MA-6233) [17]. The imaging experimental setup is illustrated in Fig. 1 and was identical for both process replicators. A polychromatic hard X-ray beam with a mean energy of ~30 keV was used. Once the incident beam passes through the sample and the powder layer, the attenuated x-ray is converted by a LuAG: Ce scintillator and emits visible light. The visible light image is magnified by a 5 × objective and then captured by a Photron FASTCAM SA-Z 2100 K camera (Photron Ltd, Japan) with 40,000 images/s framerate. The field of view (FoV) was 4.4 mm × 2.2 mm with a pixel size of 4.3 μm. Each scan track was 4 mm (PA1 substrate) and 3 mm (Al6061 substrate) in length and was centred within the FoV of the X-ray image. The process dynamics during the onset, steady state, and end of laser scanning within the sample surface and subsurface were captured, see details in [16,18].

Table 1
Chemical composition of PA1 alloy (wt%).

Elements	Al	Mn	Ni	Ce	Fe	Zr
PA1	Bal	1.84	5.5	4.6	0.3	0.3

Table 2
Chemical composition of Al6061 alloy (wt%).

Elements	Al	Mg	Si	Cu	Zn	Ti	Cr	Mn	Fe
Al6061	Bal	1.0	0.8	0.3	0.25	0.25	0.1	0.15	0.7

2.3. Image processing

The acquired radiographs were processed with ImageJ [19]. 100 flat-field images were taken prior to each set of *in situ* experiments, and the averaged image was used to correct the raw radiographs through: $FCC = \frac{I_0}{I_F}$, where FCC is the flat-field corrected image, I_0 is the raw radiograph, and I_F is the averaged flat-field image [20]. Afterwards, the stationary objects were removed by applying a custom background subtraction [21]. The pores were then segmented and quantified using ImageJ [19] built-in analysis tools, followed by applying a Gaussian filter and manual threshold value.

2.4. Microstructure characterisation

For microstructural analysis, samples were cross-sectioned, mounted, ground, and polished to a 0.25 μm finish. The microstructure, phase identification, and elemental composition were analysed using a TESCAN MAGNA Scanning Electron Microscope (SEM) equipped with an electron backscatter (BSE) detector and an Energy Dispersive X-ray (SEM-EDX) detector. AZtech and Channel5 software were used for the processing and analysis of the SEM-EDX data. An acceleration voltage of 15 eV and beam current of 1 nA were used in the characterisation.

3. Results and discussion

3.1. Microstructure

Fig. 2 shows the cross-sectional SEM microstructure of the as-built track of PBF-LB PA1 on the as-cast PA1 substrate. Many microstructural features can be distinguished between the as-built track and as-cast substrate, as shown in Fig. 2**(a)** where the as-built PBF-LB microstructure shows heterogeneous mixing of structural features compared to the large columnar intermetallics (100's of micrometres) and coarse eutectic structure in the PA1 substrate. Under PBF-LB's extremely rapid cooling (~10^6 K/s [22]), the liquid ahead of the solidification front is significantly undercooled, leading to a higher nucleation rate of the primary eutectic phase and the formation of a fine eutectic microstructure [23]. Compared to the large columnar intermetallics formed

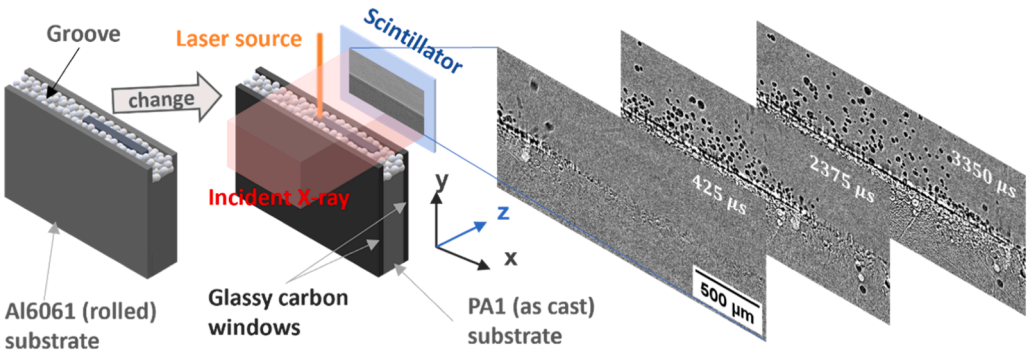

Fig. 1. Schematic of experimental set up during PBF-LB PA1 with either as-cast PA1 or as-rolled Al6061 substrates.

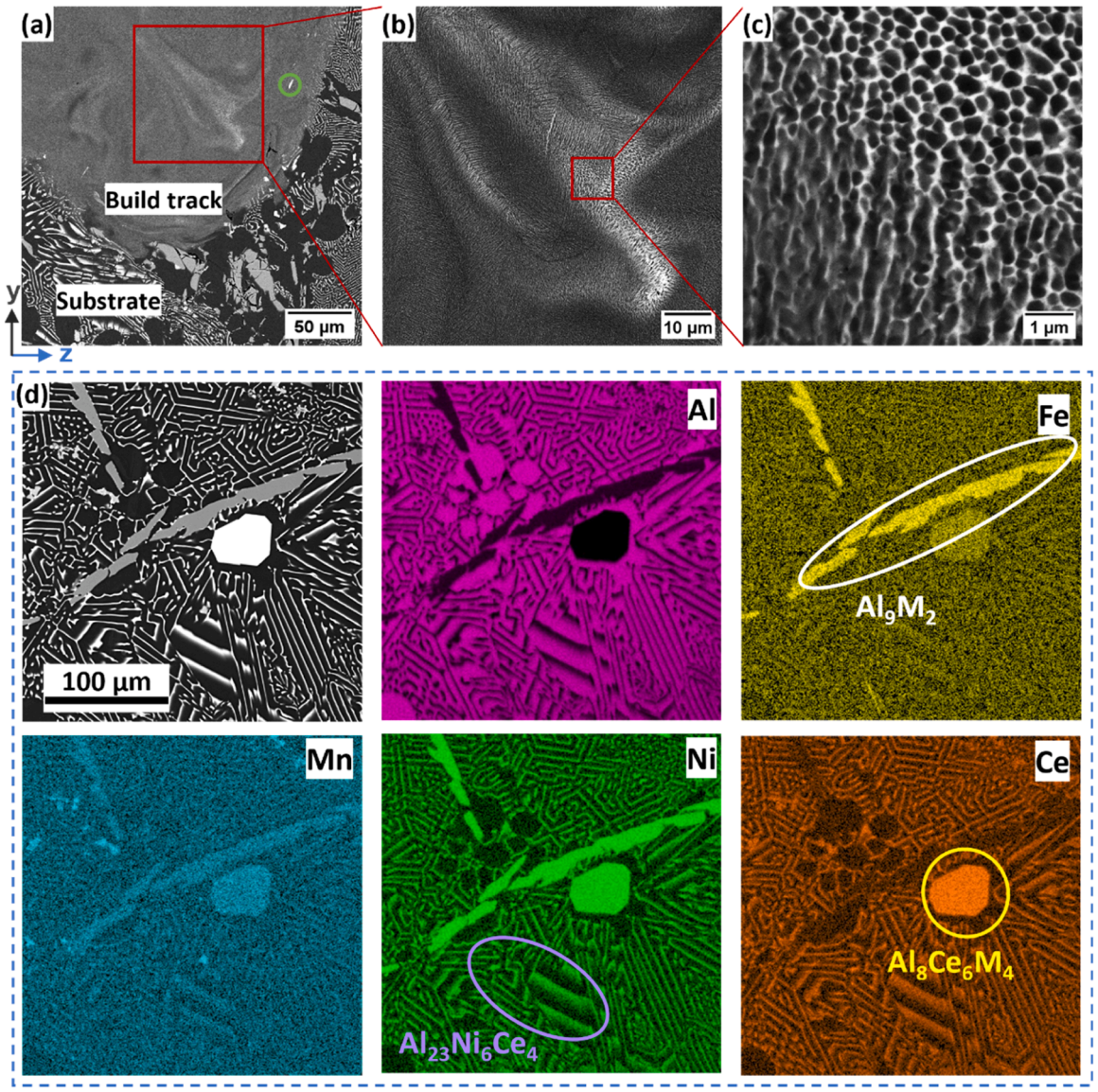

Fig. 2. Microstructure of PBF-LB manufactured PA1 on PA1 (as-cast) substrate. (a-c) SEM in different magnification showing the microstructure of both the PBF-LB track ($P = 400$ $W$and $v = 800$ mm/s) and the substrate. (d) SEM-EDX on substrate showing chemical composition distribution.

under low cooling conditions (casting), the size and number of the intermetallic is much smaller in the PBF-LB track (marked as green circle in Fig. 2**(a)** and Supplementary Fig. 1) as the rapid cooling restricts the growth of intermetallic phases.

Another consequence of rapid cooling is the elemental segregation, as shown in Fig. 2**(b)**. In this case, the large columnar intermetallics in the substrate are dissolved during PBF-LB; however, the small melt pool and high cooling rate limit diffusion/mixing distances, leading to local

segregation of the alloying elements from the intermetallic (*i.e.* Fe, Mn, Ni). This region of poorly mixed alloying elements is most evident at the bottom of the melt pool (see blue region in Supplementary Fig. 1) and are negligible in the top centre (see red region in Supplementary Fig. 1); therefore, they are not expected to propagate far into multi-layer builds.

Fig. 2**(c)** shows a magnified view of the as-built track's microstructure, exhibiting fine cellular-eutectic structure (<200 nm). In comparison, the as-cast PA1 substrate presents a mixture of large columnar intermetallics of Al_9M_2, spherical-shape intermetallics of Al_8CeM_4, and eutectic Al-$Al_{23}Ni_6Ce_4$ (see SEM-EDX analysis in Fig. 2**(d)**), where M can be Fe, Mn and/or Ni. The fraction of these phases was calculated using Scheil's equation within Thermo-calc (v. 2024b, database TCAL8) under equilibrium conditions, see Supplementary Fig. 2. As the atomic number of Ce is much higher than the other elements (Al, Fe, Ni and Mn), the large columnar intermetallic of Al_9M_2 will appear as brighter needle-shaped features in X-ray radiography compared to the Ce-rich matrix. These large columnar intermetallics in the substrate can trigger a new defect formation mode, as detailed in the following **Section 3.2**.

3.2. Defect formation

We observed and classified four types of defects during PBF-LB of PA1 on PA1 as-cast substrate according to their features and formation sequence: (i) hydrogen pores (H-pore), (ii) keyhole pores (K-pore), (iii) end-of-track defects (ETD), and (iv) intermetallic-induced pores (IM-pore). The first three (Fig. 3) are common defect types in PBF-LB whereas the IM-pore (Fig. 4) has not been previously reported in PBF-LB to our knowledge.

H-pores are one of the most common defects appearing during PBF-LB of Al alloys, due to the significant difference in hydrogen solubility between liquid (~6.9 cm^3/kg) and solid (~0.36 cm^3/kg) Al [24]. Most of the H-pores observed in this work are spherical shaped with a typical radius of < 10 μm, consistent with the results reported in ref [25]. Compared to large-sized pore that can be particularly detrimental to crack propagation, these small pores are generally considered to have a limited impact on the final built component's properties [26]. Fig. 3 **(a-c)** and **Supplementary Video V1**, show multiple small H-pores (orange solid circle) formed in the melt pool, which adhere to the surface of an existing pore and eventually coalesce to form a large H-pore with an equivalent radius of ~42 μm by minimising their surface energy. The large H-pore could be detrimental to the final properties of the PBF-LB samples.

K-pores are generated by keyhole instability [27]. Fig. 3 **(c-f)** show the keyhole dynamics (yellow dotted outline), with the significant fluctuation in keyhole morphology forming a K-pore (red dotted circle). This keyhole surface instability could lead to inconsistent internal laser reflection and uneven heating on the keyhole walls. The keyhole expands rapidly due to the localised vaporisation **(**Fig. 3 **(c))**, followed by a

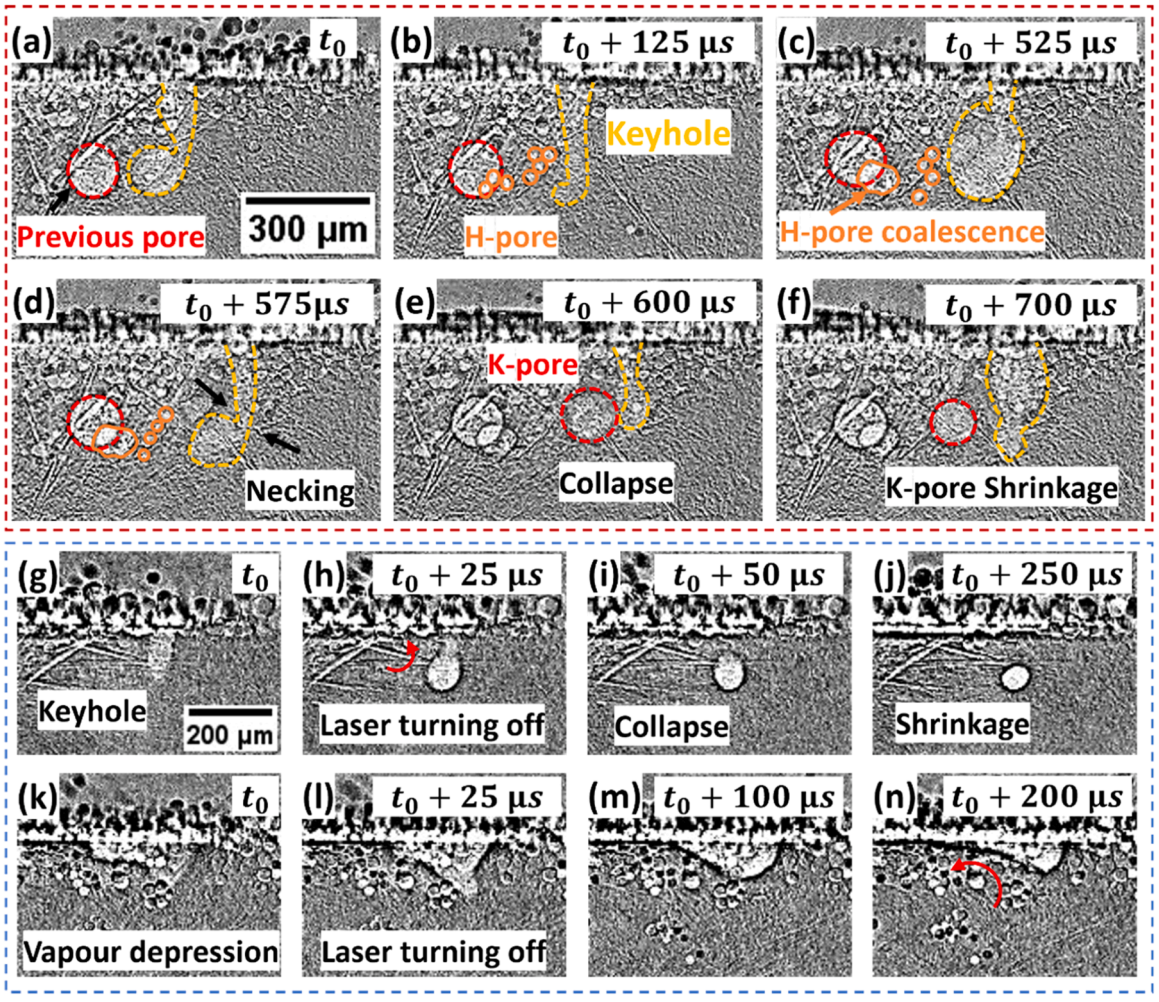

Fig. 3. X-ray images (x-y section) showing common defect formation mechanisms during PBF-LB of PA1 on PA1 (as-cast) substrate. (a-f) Formation mechanism of K-pores (red) and H-pores (orange) during PBF-LB with $P = 300$ W and $v = 250$ mm/s, where the yellow line depicts the keyhole. (g-j) Formation mechanism of end-of-track pore formation during PBF-LB with $P = 400$ W and $v = 1000$ mm/s, where the red arrow indicates the residual Marangoni flow. (k-n) Formation mechanism of end-of-track depression formation during PBF-LB with $P = 500$ W and $v = 1600$ mm/s.

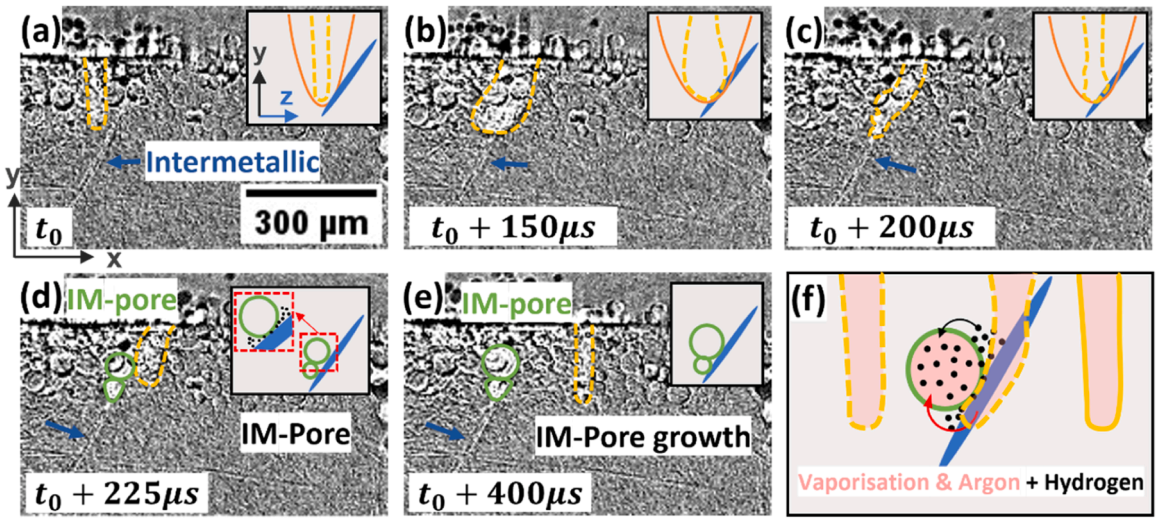

Fig. 4. Formation mechanism of a new type of defect (IM-pore): (a-e) X-ray images (x-y section) showing IM-pore (green) during PBF-LB of PA1 on as-cast PA1 substrate with $P = 300$ W and $v = 600$ mm/s. The inserts illustrate the z-y section, where blue indicates intermetallic, yellow and orange lines depicts keyhole and melt pool respectively, and black dots indicate hydrogen. (f) Schematic of IM-pore formation mechanism.

rapid shrinkage in the upper keyhole section, leading to neck formation at the mid-section of the keyhole (Fig. 3 **(d)**). The momentum transfer induced by the melt flow towards the rear of the keyhole and Plateau-Rayleigh instability [27] overcomes the surface tension of the neck region, the keyhole collapses, forming a K-pore (Fig. 3 **(e)**). The metal vapour within the K-pore condenses due to the decrease in temperature, leading to the shrinkage of the K-pore from an equivalent radius of ~65 to ~54 μm after 100 μs (Fig. 3 **(f)**), as demonstrated in ref [28].

There are two types of ETDs observed during PBF-LB of PA1: an end-of-track pore (Fig. 3 **(g-j)**) and end-of-track depression (Fig. 3 **(k-n)**). Under keyhole mode melting with 400 W power and 1000 mm/s scan speed (Fig. 3 **(g-j)**), the residual heat causes a local expansion of the keyhole (Fig. 3**(h)**) even after the laser is switched off. Then, the keyhole collapses (Fig. 3**(i)),** forming a K-pore. The outwards Marangoni flow (red arrow) within the melt pool flows upward and partially heals the top-of the keyhole cavity. A gas mixture of argon and metal vapour is trapped inside a spherical bubble in the rapidly cooling melt. As the temperature continues to cool, the bubble shrinks until the solidification front entraps it as an end-of-track pore **(**Fig. 3**(j).** The ultra-fast cooling rate (~10^6 K/s [22]) of PBF-LB leads to the rapid solidification (~0.3 m/s) of the liquid/solid interface [29].

In comparison, the end-of-track depression [30] is generated with lower input energy density (e.g. 500 W power and 1600 mm/s scan speed in Fig. 3**(k-n)**) when a depression zone has formed rather than a keyhole. As the energy density is lower, the melt pool temperature is lower and cooling is even more rapid, there is insufficient time for liquid feeding to fill the depression area before it has solidified, forming an end-of-track depression.

Apart from the commonly observed H-pore, K-pore and ETD during PBF-LB, we observed a new pore formation mechanism induced by the long needle intermetallics in the as-cast substrate, termed IM-pores (see **Supplementary Video V2)**. Fig. 4 reveals the formation mechanism of IM-pores (green solid circle) where the inserts indicate the (*z*-*y*) cross sections of the melt pool. The printing conditions with laser power of 300 W and scan speed of 600 mm/s form a stable 'I'-shaped keyhole (Fig. 4**(a)**) during PBF-LB. However, as the melt pool passes over the needle-shaped intermetallic (indicated by the blue arrow), a localised instability causes the keyhole to expand (Fig. 4**(b)**). Once the keyhole boundary encounters the intermetallic, it reduces the surface tension of the gas-liquid interface (with a gas-solid intermetallic interface). The keyhole morphology changes (Fig. 4**(c)**), and part of the keyhole adheres to the intermetallic, causing the formation of an IM-pore (Fig. 4**(d)**). Interestingly, the size of IM-pore observed in Fig. 4**(d)** grows from an equivalent radius of ~29 to ~40 μm after 175 μs (Fig. 4**(e)**).

Although the IM-pore originates from a keyhole, the presence of intermetallic compounds promotes its growth [31]. The growth of bubbles is diffusion-controlled and can be largely affected by the hydrogen concentration in the melt [32]. The intermetallic provides preferential diffusion paths, gettering hydrogen from a larger volume, increasing pore growth (Fig. 4 **(d-e)** and shown schematically in Fig. 4 **(f)**). Therefore, the entrapped gas within the IM-pore is hypothesised to be a combination of argon and metal vapour from the keyhole and hydrogen from the melt pool.

The substrate microstructure (large columnar intermetallic) effect might be most significant during the initial layers for PBF-LB builds of PA1. Its influence is expected to reduce as remelting and dilution that homogenise the microstructure. To examine this effect, multi-layers (20 layers with layer thickness of 60 μm) and multi-hatches (80 hatches with hatching distance of 150 μm to achieving hatch overlapping of ~50%) samples were produced at $P = 400W$and $v = 800mm/s$. The micrographs (see Supplementary Fig. 3) show that the initial layers present almost no intermetallic phases due to extremely rapid cooling conditions. Beyond ~10 layers, slight heat accumulation leads to reduced cooling rate and increased intermetallic formation (while with size < 1 μm), whose influence on pore formation is significantly smaller than that of the large intermetallics present in the cast substrate. However, IM-pore formation remains important for alloys, e.g. Al-Fe alloys [33,34], with needle-shaped intermetallic/precipitate formed throughout the build under AM conditions. Moreover, hybrid AM [35,36] and laser coating processing [37] require (1) printing layer directly onto conventionally manufactured blocks (which may contains large intermetallic phases), or (2) dissimilar alloy printing [38]. The interface with microstructural difference and intermetallic formation remains a critical region for IM-pore formation.

3.3. Synchrotron-derived process map

To understand the substrate influence on defect formation mechanisms during PBF-LB of PA1 Al alloy, we quantified the vapour depression morphologies across various printing conditions (laser power and scan speed combinations), producing a defect process map. Fig. 5 gives a synchrotron-derived process map of PBF-LB with PA1 powder on PA1 (as-cast) and Al6061 (rolled) substrates. A wide range of printing

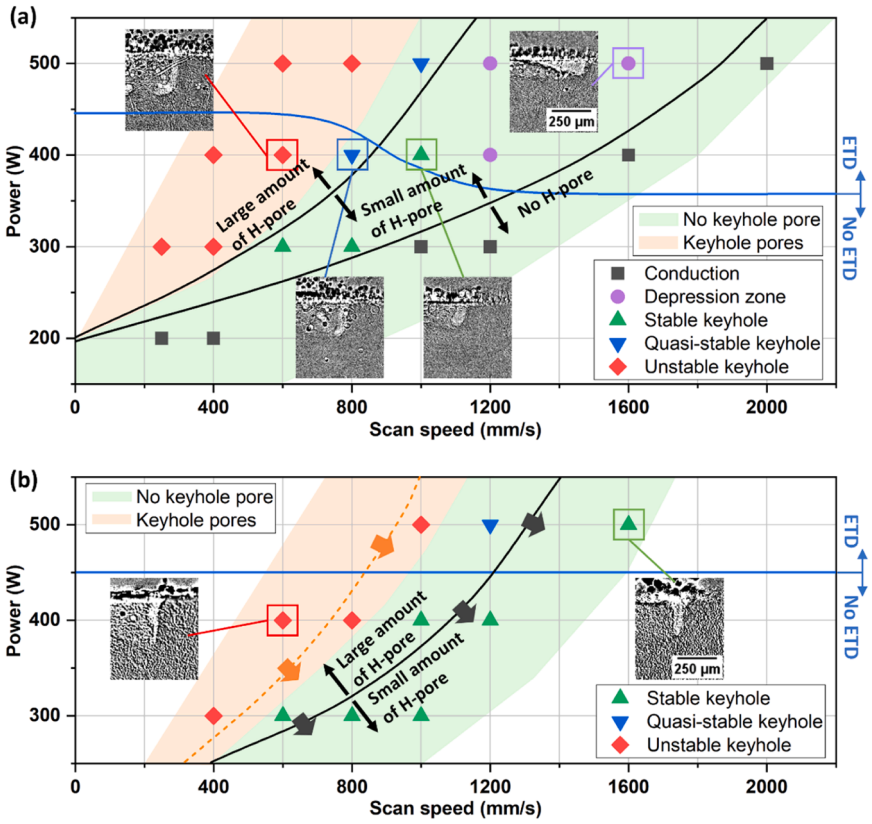

Fig. 5. Process map during PBF-LB of PA1 on (a) PA1 (as cast) substrate and (b) Al6061 (rolled) substrate, showing keyhole morphologies and defects formation.

conditions was selected for the PA1 substrate, achieving E_s from 72.2 to 30.6 $Js^{1/2}$/mm to obtain melting modes from keyhole to conduction. The observed vapour depression morphologies were unstable keyhole (red), quasi-stable keyhole (blue), stable keyhole (green), large depression zone (purple) and conduction (black). The 'unstable keyhole' is directly related to K-pore formation due to the liquid/gas interface instability, as detailed in **Section 3.2**. The 'quasi-stable' keyhole is defined as exhibiting less vigorous morphology fluctuations and no K-pore formation. A 'stable keyhole' presents a nearly constant morphology during the laser melting, also without K-pores. Compared to the high depth-to-width ratio of the keyhole, the 'depression zone' mode is shallow with a large opening area. Under the lowest E_s conditions (<37.5 $Js^{1/2}$/mm), powder denudation is observed without a vapour depression penetrating the substrate, termed as 'conduction' mode.

The K-pore and no K-pore regions for PA1 substates are shown as orange and green areas, respectively, in Fig. 5**(a)**, with the K-pore region corresponding to the unstable keyhole melting mode. The black boundaries indicate the H-pore regions. When printing with high energy in the unstable and quasi-stable keyhole modes, the number of H-pores in the enlarged pool increases significantly (>10). For medium E_s conditions (37.5–51 $Js^{1/2}$/mm), like stable keyhole or depression mode, a smaller melt pool leads to a smaller number of H-pores. When the input energy is insufficient to generate a depression zone (conduction mode), no H-pores can be observed as the melt depth is limited. The blue line indicates the ETD regions, with ETD formation under high laser power printing conditions. This might be due to the high residual heat when turning off the laser on high power. Even in conduction mode with no significant vapour depression zone, ETD can be observed with laser power higher than 400 W, due to the accumulated residual heat at the track end which causes a local expansion of the depression zone into the substrate [29], see Supplementary Fig. 4. Therefore, we suggest printing under stable keyhole (green) and depression zone (purple) conditions when performing PBF-LB of PA1, minimising defect formation.

Selected printing conditions were used during PBF-LB on Al6061 substrates for comparison, as illustrated in Fig. 5**(b)**. Similar to the as-cast PA1 substrate, the K-pores on the Al6061 substrate appear with unstable keyholes, a large number of H-pores appear with higher E_s conditions, and ETD appears with high laser power. Due to smaller laser spot size was used when printing on Al6061 substrate, the E_s is higher under the same laser power and scan speed. Therefore, we observe that the unstable keyhole region for the Al6061 substrate is shifted towards a lower E_s region (lower power and scan speed combinations), *i.e.* causing the shift of the boundaries between the K-pore/no K-pore region (orange dotted line). Similarly, the boundary between large/small amounts of the H-pore region (black line) shifts towards the lower E_s regimes. This could be due to a smaller spot size for the Al6061 runs, leading to higher power density compared to the PA1 runs, resulting in a larger melt pool in PA1 with increased dissolved hydrogen.

Due to the existence of large columnar intermetallics in the PA1 substrate, we observed IM-pores in the built tracks under all print conditions in Fig. 5, except the conduction mode (black), which has limited interaction between the laser beam and substrate. In comparison, the Al6061 (rolled) substrate exhibits fine intermetallic (with an equivalent diameter <5 μm), see SEM images in Supplementary Fig. 5. The intermetallic size is negligible compared to the melt pool size; therefore, no IM-pores were observed during PBF-LB with an Al6061 (rolled) substrate see an example in Supplementary Fig. 6, under stable keyhole mode ($P = 300W$ *and* $v = 600mm/s$).

3.4. Quantification of K-pores and IM-pores

The small-sized H-pores usually have limited influence on component quality, while large-sized K-pores [39] and IM-pores are likely to be more detrimental to the mechanical properties of the build part involving rapid cooling and intermetallic formation within the functional region of the build. To understand large pore formation across

different printing conditions, we quantified the number and total area per track unit length (mm) of K-pores and IM-pores as a function of imparted specific energy (E_s) on PA1 (as-cast) substrate (see Fig. 6). K-pore and IM-pore were distinguished manually after segmentation and quantification, according to their formation mechanism detailed in Section 2.3:

(1) IM-pores are typically formed adjacent to large intermetallic phases via keyhole attachment and deformation at the intermetallic surface, whereas K-pores are formed as a result of keyhole instability and collapse at the keyhole tip.

(2) IM-pores tend to grow after formation, combined with hydrogen gas expansion, whereas K-pores typically shrink during solidification.

As shown in Fig. 6**(a)**, both the number and total area of K-pores increase with increased E_s due to increased keyhole instability under higher imparted specific energy conditions. Note there is a E_s threshold of 65 $Js^{1/2}$/mm, above which the number and total area of K-pores double. In comparison, The number and total area of K-pores with the Al6061 substrate are significantly lower than the PA1 substrate under similar E_s conditions. Due to experimental constraints, the parameter space explored for the Al 6061 substrate is limited. Therefore, comparisons between substrates are restricted to the investigated the imparted specific energy range. When the melt pool passes through or adjacent to large columnar intermetallics in the as-cast PA1 substrate, there are localised flow perturbations in the melt pool, increasing keyhole instability and keyhole pore formation. In contrast, the Al6061 substrate with a fine microstructure and no large intermetallic shows fewer K-pores (~1.6 pores/mm track) and with a smaller size (average pore area of ~841 μm^2/mm track). While both compositional differences and substrate microstructure may influence melt pool behaviour, the observed spatial relationship between coarse intermetallic and pore initiation position indicates that substrate microstructural heterogeneity plays a significant role in IM-pore formation. However, the potential contribution of alloying elements to melt thermophysical properties cannot be excluded and would need further systematic investigation.

Unlike K-pores that are mainly controlled by the imparted specific energy, the formation of IM-pores is influenced by both the imparted specific energy and substrate conditions. Fig. 6**(b)** quantifies the number and total area of IM-pores as a function of E_s printed at 400 W laser power. As the tracks, under the same laser power, were built on the same substrate containing similar microstructure (intermetallic size and volume fraction), the number of IM-pores observed is in the same range, even across different scan speeds. For example, the IM-pore number is approximately 1.75/mm track with 400 W power in Fig. 6**(b)** compared to below 1/mm track with 300 W power (see Supplementary Fig. 7). Regardless of the substrate influence, the number and total area of IM-pores increase with an increase E_s in each case. This is due to the increased energy input leading to a larger keyhole/depression zone and melt pool, which could allow a greater chance of interaction with the intermetallics to form more IM-pores. In addition, the larger melt pool contains more hydrogen, enhancing IM-pore growth. Therefore, the average IM-pore size is expected to be larger with increased energy input.

4. Conclusions

We have designed a eutectic Al alloy, PA1, based on the Al-Ni-Ce-Mn-Fe alloy system for AM applications. Microstructural analysis revealed that PA1 produced by PBF-LB exhibits an extremely fine eutectic structure of ~200 nm. To better understand the influence of the substrate microstructure on printability and defect formation, we employed high-speed *in situ* synchrotron X-ray imaging to capture melt pool dynamics during PBF-LB. Four distinct defect types were identified, including a newly discovered defect, termed IM-pore, which forms when the keyhole interacts with large columnar intermetallic phases in the substrate. Additionally, we quantify the number and total area of large K-pores and IM-pores under various processing conditions and substrate types. The large intermetallics in the substrate can induce IM-pore formation; therefore, post-processing of the substrate including rolling or heat treatment that can homogenise the microstructure could be beneficial. By establishing process maps, we demonstrate that using optimised parameter can minimise defect formation and enable the production of high-quality components for both substrates. The

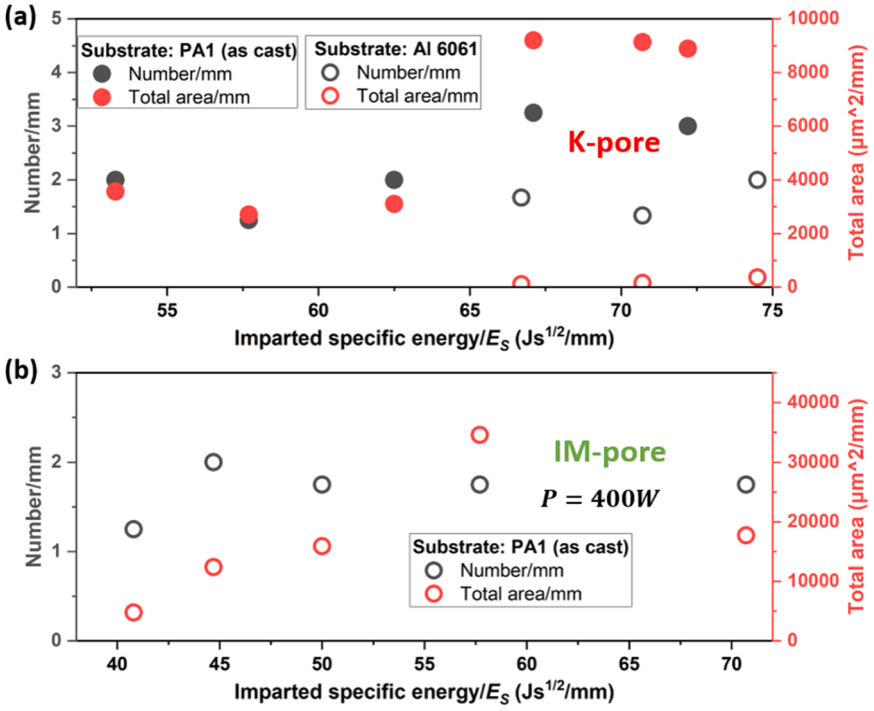

Fig. 6. *Quantification of pore number and total area as a function of imparted specific energy (E_s)* during PBF-LB of PA1, for (a) quantification of K-pore on PA1(as cast) and Al 6061 (rolled) substrate and (b) quantification of IM-pore with laser power of 400 W on PA1(as cast) substrate.

optimised parameters may shift with different substrate types, but consistently lies at moderate energy inputs with stable keyhole and vapour depression regimes. This *in situ* study focuses on single-track AM conditions to isolate the fundamental mechanisms governing melt pool behaviour and intermetallic-melt interactions. To evaluate the microstructure influence on practical LPBF builds, complementary multi-layers and multi-hatches build of PA1 under certain condition was also examined and discussed. A systematic investigation of fully three-dimensional builds and their resulting microstructure and mechanical properties will be pursued in future work to further validate the process–structure–property relationship.

CRediT authorship contribution statement

Dmitry G. Eskin: Writing – review & editing, Supervision, Investigation, Funding acquisition. **Iakovos Tzanakis:** Writing – review & editing, Supervision, Investigation, Funding acquisition. **Federico Sket:** Writing – review & editing, Methodology, Investigation, Funding acquisition, Data curation, Conceptualization. **Steven Van Petegem:** Writing – review & editing, Methodology, Investigation, Funding acquisition, Conceptualization. **Shishira Bhagavath:** Writing – review & editing, Methodology, Investigation, Formal analysis. **Rubén Lambert-Garcia:** Writing – review & editing, Methodology, Investigation, Formal analysis. **Peter D. Lee:** Writing – review & editing, Supervision, Investigation, Funding acquisition, Conceptualization. **Da Guo:** Writing – original draft, Methodology, Investigation, Formal analysis, Data curation, Conceptualization. **Chu Lun Alex Leung:** Writing – review & editing, Supervision, Investigation, Funding acquisition, Conceptualization. **Chengbo Zhu:** Writing – original draft, Methodology, Investigation, Formal analysis, Data curation. **Marta Majkut:** Methodology, Investigation, Data curation. **Alexander Rack:** Writing – review & editing, Methodology, Investigation, Data curation. **Sebastian Marussi:** Methodology, Investigation, Data curation.

Declaration of Competing Interest

The authors declare that they have no known competing financial interests or personal relationships that could have appeared to influence the work reported in this paper.

Acknowledgement

The authors acknowledge the support from the UKRI—EPSRC, Grants Numbered EP/W006774/1, EP/P006566/1, EP/W003333/1, EP/V061798/1 and EP/W522193/1. PDL is funded by the support from a Royal Academy of Engineering Chair in Emerging Technologies (CiET1819/10); CLAL is funded in part by EP/W037483/1 and IPG Photonics/ Royal Academy of Engineering Senior Research Fellowship in SEARCH (ref: RCSRF2324–18–71). SVP acknowledges funding from the ETH Domain via the SFA-AM MULTIMAT project and from the Swiss National Science Foundation (SNSF, grant No. 193799). The atomization of powder was done by a proprietary ultrasonic atomization technology developed and implemented by Amazemet Sp. z o.o. This research used resources of the European Synchrotron Radiation Facility (ESRF) in Beamline ID19 under two proposal ME-1573 and MA-6233. Many thanks to team members from the Multiscale X-ray Imaging Lab at Harwell (MXI Lab) for their assistance in preparation for and during the beamtime. Special thanks to Andaç Özsoy for the training on the miniSLM and William Hearn for help during the measurements.

Appendix A. Supporting information

Supplementary data associated with this article can be found in the online version at doi:10.1016/j.addma.2026.105229.

Data availability

Data will be made available on request.

References

[1] E. MacDonald, R. Wicker, Multiprocess 3D printing for increasing component functionality, Science 353 (6307) (2016) aaf2093.
[2] L. Zhao, L. Song, J.G. Santos Macías, Y. Zhu, M. Huang, A. Simar, Z. Li, Review on the correlation between microstructure and mechanical performance for laser powder bed fusion AlSi10, Mg. Addit. Manuf. 56 (2022) 102914.
[3] C. Dan, Y. Cui, Y. Wu, Z. Chen, H. Liu, G. Ji, Y. Xiao, H. Chen, M. Wang, J. Liu, L. Wang, Y. Li, A. Addad, Y. Zhou, S. Ma, Q. Shi, H. Wang, J. Lu, Achieving ultrahigh fatigue resistance in AlSi10Mg alloy by additive manufacturing, Nat. Mater. 22 (10) (2023) 1182–1188.
[4] P.A. Rometsch, et al., Review of high-strength aluminium alloys for additive manufacturing by laser powder bed fusion, Mater. & Des. 219 (2022) 110779.
[5] J.H. Martin, B.D. Yahata, J.M. Hundley, J.A. Mayer, T.A. Schaedler, T.M. Pollock, 3D printing of high-strength aluminium alloys, Nature 549 (7672) (2017) 365–369.
[6] D.T. Rees, et al., situ X-ray imaging of hot cracking and porosity during LPBF of Al-2139 with TiB2 additions and varied process parameters, Mater. & Des. 231 (2023) 112031.
[7] Zhu, C., et al., *Design of Hot-Tearing Resistant and Thermally Stable Aluminium Alloys for Advanced Casting Technologies*. Available at SSRN 5445794, 2025.
[8] A. Shang, B. Stegman, K. Choy, T. Niu, C. Shen, Z. Shang, X. Sheng, J. Lopez, L. Hoppenrath, B.P. Zhang, H. Wang, P. Bellon, X. Zhang, Additive manufacturing of an ultrastrong, deformable Al alloy with nanoscale intermetallics, Nat. Commun. 15 (1) (2024) 5122.
[9] D. Guo, C. Zhu, H.E. Chapman, K. Zhang, W. Li, S. Bhagavath, R. Atwood, S. Michalik, D.G. Eskin, I. Tzanakis, C.L.A. Leung, P.D. Lee, Mechanical and in situ thermal-related behavior upon directed energy deposition additive manufacturing of a high-performance Al alloy, Int. J. Extrem. Manuf. 8 (2026) 035002.
[10] A. Abdali, S. Hossein Nedjad, H. Hamed Zargari, A. Saboori, M. Yildiz, Predictive tools for the cooling rate-dependent microstructure evolution of AISI 316L stainless steel in additive manufacturing, J. Mater. Res. Technol. 29 (2024) 5530–5538.
[11] C. Puncreobutr, P.D. Lee, K.M. Kareh, T. Connolley, J.L. Fife, A.B. Phillion, Influence of Fe-rich intermetallics on solidification defects in Al–Si–Cu alloys, Acta Mater. 68 (2014) 42–51.
[12] J. Wang, M. Li, J. Allison, P.D. Lee, Multiscale modeling of the influence of Fe content in a Al–Si–Cu alloy on the size distribution of intermetallic phases and micropores, J. Appl. Phys. 107 (6) (2010) 061804.
[13] C.L.A. Leung, D. Luczyniec, E. Guo, S. Marussi, R.C. Atwood, M. Meisnar, B. Saunders, P.D. Lee, Quantification of interdependent dynamics during laser additive manufacturing using x-ray imaging informed multi-physics and multiphase simulation, Adv. Sci. 9 (36) (2022) 2203546.
[14] S. Hocine, et al., Physical twin of an industrial quad-laser powder bed fusion machine for high-speed multi-modal sensing measurements, Mater. & Des. 252 (2025) 113767.
[15] C. Iantaffi, C.L.A. Leung, G. Maddison, E. Bele, S. Hocine, R. Snell, A. Rack, M. Meisnar, T. Rohr, I. Todd, P.D. Lee, Laser additive manufacturing of lunar regolith simulant: New insights from in situ synchrotron X-ray imaging, Addit. Manuf. 101 (2025) 104711.
[16] S. Hocine, H. Van Swygenhoven, S. Van Petegem, C.S.T. Chang, T. Maimaitiyili, G. Tinti, D. Ferreira Sanchez, D. Grolimund, N. Casati, Operando X-ray diffraction during laser 3D printing, Mater. Today 34 (2020) 30–40.
[17] T. Weitkamp, P. Tafforeau, E. Boller, P. Cloetens, J.P. Valade, P. Bernard, F. Peyrin, W. Ludwig, L. Helfen, J. Baruchel, M. Denecke, C.T. Walker, Status and evolution of the ESRF beamline ID19, AIP Conf. Proc. 1221 (1) (2010) 33–38.
[18] W. Li, R. Lambert-Garcia, A.C.M. Getley, K. Kim, S. Bhagavath, M. Majkut, A. Rack, P.D. Lee, C.L.A. Leung, AM-SegNet for additive manufacturing in situ X-ray image segmentation and feature quantification, Virtual Phys. Prototyp. 19 (1) (2024) e2325572.
[19] J. Schindelin, I. Arganda-Carreras, E. Frise, V. Kaynig, M. Longair, T. Pietzsch, S. Preibisch, C. Rueden, S. Saalfeld, B. Schmid, J.Y. Tinevez, D.J. White, V. Hartenstein, K. Eliceiri, P. Tomancak, A. Cardona, Fiji: an open-source platform for biological-image analysis, Nat. Methods 9 (7) (2012) 676–682.
[20] C.L.A. Leung, S. Marussi, R.C. Atwood, M. Towrie, P.J. Withers, P.D. Lee, situ X-ray imaging of defect and molten pool dynamics in laser additive manufacturing, Nat. Commun. 9 (1) (2018) 1355.
[21] D. Guo, R. Lambert-Garcia, S. Hocine, X. Fan, H. Greenhalgh, R. Shahani, M. Majkut, A. Rack, P.D. Lee, C.L. Alex Leung, Correlative spatter and vapour depression dynamics during laser powder bed fusion of an Al-Fe-Zr alloy, Int. J. Extrem. Manuf. 6 (5) (2024) 055601.
[22] P.A. Hooper, Melt pool temperature and cooling rates in laser powder bed fusion, Addit. Manuf. 22 (2018) 548–559.
[23] A. Prasad, L. Yuan, P. Lee, M. Patel, D. Qiu, M. Easton, D. StJohn, Towards understanding grain nucleation under Additive Manufacturing solidification conditions, Acta Mater. 195 (2020) 392–403.
[24] H. Toda, T. Hidaka, M. Kobayashi, K. Uesugi, A. Takeuchi, K. Horikawa, Growth behavior of hydrogen micropores in aluminum alloys during high-temperature exposure, Acta Mater. 57 (7) (2009) 2277–2290.
[25] R. Xu, et al., Towards the hydrogen pore in additively manufactured AlMgScZr alloy: Influencing factors, formation kinetics mechanism, J. Mater. Sci. & Technol. 199 (2024) 125–144.

[26] W.H. Kan, L.N.S. Chiu, C.V.S. Lim, Y. Zhu, Y. Tian, D. Jiang, A. Huang, A critical review on the effects of process-induced porosity on the mechanical properties of alloys fabricated by laser powder bed fusion, J. Mater. Sci. 57 (21) (2022) 9818–9865.
[27] X. Fan, T.G. Fleming, S.J. Clark, K. Fezzaa, A. Getley, S. Marussi, H. Wang, C. Leung, A. Kao, P.D. Lee, Magnetic modulation of keyhole instability during laser welding and additive manufacturing, Science 387 (6736) (2025) 864–869.
[28] Y. Huang, T.G. Fleming, S.J. Clark, S. Marussi, K. Fezzaa, J. Thiyagalingam, C. Leung, P.D. Lee, Keyhole fluctuation and pore formation mechanisms during laser powder bed fusion additive manufacturing, Nat. Commun. 13 (1) (2022) 1170.
[29] A.A. Martin, N.P. Calta, S.A. Khairallah, J. Wang, P.J. Depond, A.Y. Fong, V. Thampy, G.M. Guss, A.M. Kiss, K.H. Stone, C.J. Tassone, J. Nelson Weker, M. F. Toney, T. van Buuren, M.J. Matthews, Dynamics of pore formation during laser powder bed fusion additive manufacturing, Nat. Commun. 10 (1) (2019) 1987.
[30] E. Ruckh, R. Lambert-Garcia, S. Hocine, A.C.M. Getley, C. Iantaffi, A. Bhatt, M. Fitzpatrick, S. Marussi, A. Farndell, T. Schubert, G. Ketzer-Raichle, M. Majkut, A. Rack, N. Jones, C.L.A. Leung, P.D. Lee, Process mapping of Ti-6Al-4V laser powder bed fusion using in situ high-speed synchrotron x-ray imaging, Addit. Manuf. 113 (2025) 105007.
[31] S. Sun, Q. Hu, W. Lu, Z. Ding, M. Xia, J. Li, Situ observation on bubble behavior of solidifying al-ni alloy under the interference of intermetallic compounds, Metall. Mater. Trans. A 49 (10) (2018) 4429–4434.
[32] R.C. Atwood, S. Sridhar, W. Zhang, P.D. Lee, Diffusion-controlled growth of hydrogen pores in aluminium–silicon castings: in situ observation and modelling, Acta Mater. 48 (2) (2000) 405–417.
[33] C. Shen, Z. Pan, Y. Ma, D. Cuiuri, H. Li, Fabrication of iron-rich Fe–Al intermetallics using the wire-arc additive manufacturing process, Addit. Manuf. 7 (2015) 20–26.
[34] W. Wang, N. Takata, A. Suzuki, M. Kobashi, M. Kato, Formation of multiple intermetallic phases in a hypereutectic Al–Fe binary alloy additively manufactured by laser powder bed fusion, Intermetallics 125 (2020) 106892.
[35] V.V. Popov, A. Fleisher, Hybrid additive manufacturing of steels and alloys, Manuf. Rev. 7 (2020) 6.
[36] H. Azizi, R. Ghiaasiaan, R. Prager, M.H. Ghoncheh, K.A. Samk, A. Lausic, W. Byleveld, A.B. Phillion, Metallurgical and mechanical assessment of hybrid additively-manufactured maraging tool steels via selective laser melting, Addit. Manuf. 27 (2019) 389–397.
[37] V. Glushych, K. Kallies, M. Zimmermann, H. Betsch, B. Vieland, C. Henk, T. Schopphoven, W. Meiners, Surface modification by combining extreme high-speed laser material deposition (EHLA) with simultaneous roller burnishing, J. Laser Appl. 37 (4) (2025) 042026.
[38] Z.H. Liu, D.Q. Zhang, S.L. Sing, C.K. Chua, L.E. Loh, Interfacial characterization of SLM parts in multi-material processing: Metallurgical diffusion between 316L stainless steel and C18400 copper alloy, Mater. Charact. 94 (2014) 116–125.
[39] Z. Yang, W. Wang, Y. Chen, S. Wang, G. Bian, L. Lan, Z. Zhao, H. Zhang, C. Li, X. Wang, An experimental and numerical study on the evolution of pores and its effect on the tensile properties of LPBF Invar36 with different energy density, J. Mater. Res. Technol. 31 (2024) 3064–3078.